THE JOURNAL OF PHYSICAL CHEMISTRY C
A JOURNAL OF THE AMERICAN CHEMICAL SOCIETY

pubs.acs.org/JPCC

Article

Optimizing SO_2–Promoted NO Oxidation over Single-Atom Catalysts via Activity Volcano Plot

Zhengyang Gao, Ze Liu, Chu Wang, Ziwei Miao, Tongao Yao, Jianghao Cai, Yixiao Sun, Yuanzheng Qu, and Weijie Yang*

Cite This: J. Phys. Chem. C 2026, 130, 2538–2548

Read Online

ACCESS | Metrics & More | Article Recommendations | Supporting Information

ABSTRACT: Catalytic oxidation represents a predominant strategy for NO abatement. While SO_2 has been recognized as a critical promoter of NO oxidation, the fundamental principles governing catalytic performance and robust descriptors for material selection remain inadequately explored. Herein, we investigate the catalytic oxidation of NO with HSO_3 as the oxidant over transition metal single-atom catalysts (TM-N_4–C, TM = V ∼ Zn) through density functional theory (DFT) calculations. For HSO_3 generation, the energy barriers showed minimal variation among catalysts, providing an insufficient basis for screening. Thus, we focused on the critical HSO_3-mediated NO oxidation step (HSO_3 + NO → SO_2 + HNO_2). Using the Brønsted–Evans–Polanyi relationship and microkinetic modeling, we established HSO_3 adsorption energy as a descriptor and constructed a catalytic activity volcano plot. Notably, through screening 3d-5d transition metal single-atom catalysts identified Co–N_4–C as the most active catalyst, which exhibits an optimal balance between a moderate 0.42 eV energy barrier and weak 0.43 eV Co-SO_2 interaction. Subsequently, fixed-bed experiments performed on the theoretically screened optimal catalyst (Co–N_4–C) confirmed the significant promotional effect of SO_2, demonstrating that appropriate SO_2 concentrations effectively enhance NO oxidation via the HSO_3-mediated pathway. This work elucidates the fundamental promotion mechanism of SO_2 and establishes a descriptor-based framework for the rational design of high-performance NO oxidation catalysts.

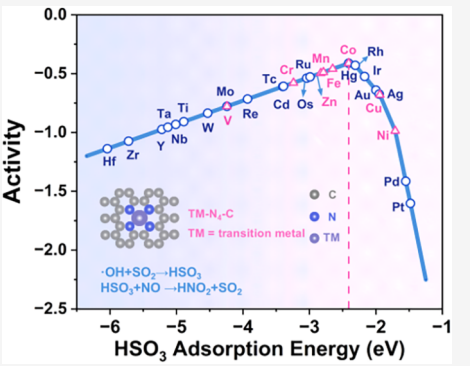

1. INTRODUCTION

Nitric oxide (NO) is a predominant atmospheric pollutant emitted from coal-fired power plants and industrial boilers. It not only poses significant threats to human health but also adversely impacts ecosystems. Consequently, the development of efficient purification technologies for NO has remained a key research focus in the field of environmental catalysis.[1,2] At present, catalytic oxidation stands out as a promising strategy for pollutant removal, showing exceptional potential in NO removal.[3,4] Notably, SO_2 is a common flue gas component that amplifies NO oxidation efficiency by modifying reaction pathways in specific catalytic systems.[5,6] Nevertheless, the synergistic mechanism of SO_2 in NO removal remains incompletely understood, and the existing catalysts fail to fully exploit the promoting effects of SO_2 on NO, limiting further improvements in denitrification efficiency.[7−9] Therefore, investigating the enhancement mechanism of SO_2 and developing catalysts that can effectively harness its facilitating effect on NO removal are of significant importance.

Advanced oxidation processes (AOPs) achieve efficient pollutant degradation through in situ generation of reactive oxygen species, offering advantages such as robust oxidative power, fast reaction kinetics, and minimal environmental impact.[10,11] As a representative oxidant, hydrogen peroxide (H_2O_2) is widely employed due to its cost-effectiveness and environmental benignity. Although H_2O_2 exhibits moderate reactivity in its native state, proper activation can generate highly reactive hydroxyl radicals (•OH), enabling efficient degradation of refractory pollutants.[12] This characteristic makes H_2O_2-based AOPs particularly promising for environmental remediation applications. Researchers have developed diverse synthetic strategies to engineer H_2O_2-activating catalysts for nitrogen oxide (NO) oxidation. Chen et al.[13] fabricated Pt/TiO_2 catalysts through an impregnation-reduction method, demonstrating that optimal Pt loading enhances both H_2O_2 chemisorption and activation, consequently boosting •OH generation for efficient NO oxidation. Similarly, Wu et al.[14] investigated $La_{1-x}Ca_xFeO_3$ perovskites (x = 0–0.5) for H_2O_2 decomposition and found that $LaFeO_3$ (x = 0) exhibited the highest catalytic activity in the series, achieving 89.9% NO conversion under optimized conditions. Their

Received: November 9, 2025
Revised: January 7, 2026
Accepted: January 30, 2026
Published: February 5, 2026

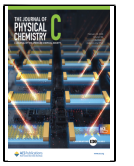

https://doi.org/10.1021/acs.jpcc.5c07658
J. Phys. Chem. C 2026, 130, 2538–2548

characterization results indicated that gradual Ca substitution led to concurrent increases in surface hydroxyl density and oxygen vacancy concentration. Notably, oxygen vacancies predominantly exhibited a negative effect on •OH generation and subsequent NO removal, as they promoted H_2O_2 decomposition without yielding •OH radicals. These insights highlight the pivotal role of •OH radicals in advanced oxidation processes (AOPs), offering critical guidance for catalytic system optimization. The underlying mechanism not only explains performance variations among different catalytic materials but also provides a theoretical foundation for designing high-efficiency AOP systems.[15] Among •OH generation methods, H_2O_2 decomposition over solid catalysts has emerged as a practical and effective approach, achieving high pollutant removal efficiency in flue gas treatment.[16] Therefore, developing advanced catalytic materials to create an efficient NO oxidation platform for complex flue gases is of significant importance.

Single-atom catalysts (SACs) have emerged as frontier materials in catalytic oxidation due to their exceptional atom efficiency, tunable active sites, and remarkable antipoisoning properties.[17−19] The chemical inertness of graphene supports enables precise electronic modulation of anchored metal sites through strategic doping,[20] which has been shown to impart outstanding NO oxidation activity through optimized electronic configurations and maximal atomic utilization. For instance, Liu et al.[21] systematically investigated the oxidation mechanisms of NO and Hg^0 on Pd single-atom catalysts supported on g-C_3N_4 (Pd SAC/g-C_3N_4), revealing relatively low reaction barriers (0.46 eV for NO oxidation and 1.81 eV for Hg^0 oxidation), indicative of superior low-temperature catalytic performance. Yang et al.[22] employed density functional theory (DFT) calculations to investigate NO reduction on Fe-embedded monovacancy graphene (Fe/MG), identifying a Langmuir−Hinshelwood mechanism with an activation barrier of 0.81 eV, which confirms its high catalytic efficiency. Notably, the presence of SO_2 profoundly enhances catalytic NO oxidation by altering H_2O_2 decomposition pathways.[23] Experimental work with $Fe_2(SO_4)_3$[24] and $Fe/Al_2O_3@SiO_2$[25] catalysts confirmed substantially higher NO conversion rates in SO_2-containing environments compared to SO_2-free conditions. Moreover, our earlier work elucidated the mechanism of SO_2-promoted H_2O_2 oxidation over the Fe−N_4−C catalyst, demonstrating that HSO_3 intermediates are crucial for highly efficient NO oxidation.[26] However, a generalizable descriptor for the catalytic activity across diverse metal centers and the electronic-structure origin of the SO_2 promotion effect remain unexplored. Herein, we extend the investigation to 28 TM-N_4−C catalysts (TM = 3d, 4d, 5d metals) and establish the HSO_3 adsorption energy as a universal descriptor. Using this descriptor, we develop an activity volcano plot that identifies Co−N_4−C as the optimal catalyst. Furthermore, we reveal the electronic-structure basis of the promotion mechanism, thereby providing a robust framework for rational catalyst design.

In this work, we systematically investigated the SO_2-promoted NO oxidation mechanism over eight transition metal single-atom catalysts (TM-N_4−C, TM = V ∼ Zn) through spin-polarized DFT calculations. Initially, we examined HSO_3 formation pathways across the eight TM-N_4−C catalysts, uncovering the geometric configurations of critical reaction intermediates and their energetic profiles. Subsequently, we calculated the NO oxidation process by HSO_3 on all eight TM-N_4−C catalysts, obtaining linear relationships between HSO_3 adsorption energy and the reaction energy barrier, and the SO_2 desorption energy barrier. Through microkinetic modeling of 28 3d, 4d, and 5d transition metal SACs, we constructed an activity volcano plot for NO oxidation using HSO_3 adsorption energy as the descriptor, identifying Co−N_4−C as the optimal catalyst located near the volcano apex. Based on the theoretical screening results, the Co−N_4−C catalyst was synthesized and evaluated in fixed-bed experiments. Moreover, electronic structure analysis was performed to elucidate the correlation between the electronic properties and catalytic activity. The fundamental structure−activity correlations developed in this work establish a robust framework for designing and selecting high-efficiency NO oxidation catalysts.

2. CALCULATION AND EXPERIMENTS

2.1. DFT Calculation

The quantum mechanical calculations presented in this work were implemented within the framework of density functional theory (DFT), utilizing the Vienna Ab Initio Simulation Package (VASP). we adopted the projector augmented wave (PAW) pseudopotential approach throughout all simulations.[27] To properly describe exchange-correlation effects, our calculations incorporated the Perdew−Burke−Ernzerhof (PBE) generalized gradient approximation (GGA) functional, supplemented with the DFT-D3 correction scheme to account for van der Waals interactions.[28−30] The catalyst was modeled using a $5 \times 3\sqrt{3} \times 1$ graphene supercell with a 20 Å vacuum layer to prevent periodic interactions.[31] Geometry optimization procedures were conducted with careful attention to numerical convergence parameters. The Brillouin zone integration was sampled using a Γ-centered $2 \times 2 \times 1$ *k*-point mesh, coupled with a plane-wave basis set cutoff energy of 450 eV to ensure complete convergence of the electronic wave functions (Figure S1). Atomic positions were relaxed until the maximum residual force on any atom fell below the stringent threshold of 0.02 eV $Å^{-1}$. For subsequent electronic structure analysis, we increased the k-point sampling density to $4 \times 4 \times 1$ and enforced an electronic self-consistency criterion of 10^{-5} eV. To precisely monitor the electron transfer behavior during the reaction, the charge distribution was analyzed using the Bader charge analysis approach.[32] Concurrently, the bonding stability in the model was examined through the projected crystal orbital Hamiltonian population (pCOHP)[33] method in conjunction with the LOBSTER computational tool.[34]

The determination of reaction pathways and activation barriers employed a dual-methodology approach combining the climbing-image nudged elastic band (CI-NEB)[35] technique with the improved dimer method (IDM).[36] During these calculations, we enforced a tightened force convergence criterion of 0.05 eV/Å. Minimum-energy configurations and transition states were confirmed via vibrational frequency analysis, with atomic displacements constrained to ±0.02 Å.[37] The calculation equations of binding energy, adsorption energy, energy barrier, and electronegativity were provided in the S1 and S2. Furthermore, the Gibbs free energies of all intermediates and transition states were calculated by considering zero-point energy, enthalpy, and entropy contributions from vibrational frequency analysis (see SI S1). The activity volcano plot was constructed through Sabatier

https://doi.org/10.1021/acs.jpcc.5c07658
J. Phys. Chem. C 2026, 130, 2538−2548

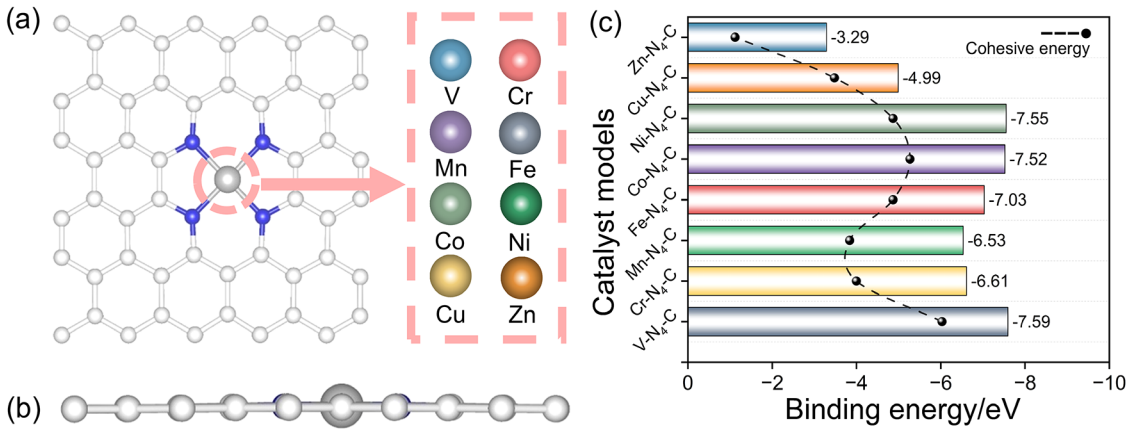

Figure 1. (a) Top and (b) side views of the SACs configuration. (c) Binding and cohesive energies of 8 types of TM-N_4−C (TM = V ∼ Zn) catalysts. C, N, and TM atoms are represented by white, blue, and gray colors, respectively.

microkinetic modeling, in which the activity is derived from the Sabatier rate-taken as the slowest step among R2-R4, with step R1 assumed to be in quasi-equilibrium. Further kinetic equations and coverage details are provided in SI S2.

2.2. Verification Experiments

To validate the accuracy of the catalyst screening results predicted by the activity volcano plot, fixed-bed experiments were conducted. The experiment were carried out under simulated flue gas conditions with a total flow rate of 1 L/min, in which the O_2 content was 6 vol % and the NO concentration was 500 ppm. The NO removal efficiency was monitored as a function of time by systematically varying the SO_2 concentration (0, 200 ppm). The catalytic reaction was carried out in a quartz tube reactor (diameter 10 mm, length 300 mm) packed with 0.1 g of catalyst (for materials information in S3, preparation and characterization details in S4) and maintained at 140 °C. Simultaneously, 3 wt % H_2O_2 solution was continuously vaporized at a flow rate of 250 μL/min and introduced into the reactor using N_2 as the carrier gas. The reaction products were dried with anhydrous $CaCl_2$ to remove moisture before real-time NO concentration monitoring using a flue gas analyzer (MRU). All gas lines were heated to 140 °C to prevent H_2O_2 condensation. This system configuration ensured uniform gas-catalyst contact while enabling precise control of reaction conditions. Further details of the experimental apparatus are provided in Figure S2. The removal efficiency of NO (η) is calculated according to the following equation

$$\eta\ (\%) = \frac{C_{inlet} - C_{outlet}}{C_{inlet}} \times 100\% \quad (1)$$

where C_{inlet} is the inlet concentration of NO; and C_{outlet} is the outlet concentration of NO.

3. RESULTS AND DISCUSSION

3.1. Catalyst Model

Previous studies have established that single-atom catalysts supported on tetra-nitrogen-doped graphene (N_4-G) substrates exhibit remarkable structural stability.[38] Therefore, we designed a series of carbon-based SACs by anchoring eight 3d transition metals (TM = V ∼ Zn) at N_4-vacancy sites.[39] The optimized geometries of the TM-N_4−C configurations are presented in Figure 1a (top view) and 1b (side view). To evaluate structural stability, we calculated the binding energies ($|E_b|$) for all catalysts (Figure 1c). Stability is determined by comparing $|E_b|$ with the metal's cohesive energy ($|E_{coh}|$, represented by dashed lines in Figure 1c). All catalysts satisfy $|E_b| > |E_{coh}|$, confirming their thermodynamic stability.

3.2. Reaction Pathways Analysis

Having established the structural stability of these SACs, we next examined their catalytic performance for NO oxidation. The sulfur in SO_2 exhibits a +4 oxidation state, displaying strong reducing ability. This property promotes SO_2 adsorption on the catalyst surface, where it subsequently reacts with radicals to form adsorbed high-valence species such as SO_3, SO_4^{2-}, HSO_3, and HSO_4.[40] Moreover, we speculate that these intermediates exhibit strong adsorption energy and considerable oxidation capacity on TM-N_4−C catalyst. Based on our previous studies, NO is most likely oxidized by HSO_3, with HNO_2 being the final product, as this pathway presents the lowest energy barrier for the rate-determining step.[26] Therefore, we investigated the reaction pathway of NO oxidation by sulfur-containing intermediates (HSO_3) to form HNO_2 on single-atom catalysts (SACs). Considering HSO_3 as the oxidant for NO catalytic conversion, the overall reaction process can be divided into the following steps: (1) The $^{\bullet}$OH radicals generated from H_2O_2 activation adsorb on the catalyst's active sites, where they react with SO_2 to form HSO_3. (2) NO reacts with HSO_3, producing SO_2 and HNO_2, which desorbs from the surface.

3.2.1. Reaction Pathways for HSO_3 Formation on SACs. To uncover the mechanistic role of SO_2 in promoting NO oxidation, we initially explored the formation of the key intermediate HSO_3. Although subsequent screening identified Co−N_4−C as the most active catalyst, we employed the Fe−N_4−C system as a representative model in the following sections to uncover the reaction mechanisms. This choice is based on its well-established status in prior studies and the representative nature of its reaction pathways across the TM-N_4−C series.[26] As shown in Figure 2a, the reaction mechanism of HSO_3 formation from adsorbed $^{\bullet}$OH and gaseous SO_2 on the Fe−N_4−C catalyst was systematically examined. First, the $^{\bullet}$OH radical generated from H_2O_2 activation preferentially occupies the metal site of the Fe−N_4−C catalyst, forming a stable adsorption configuration (IM0), as its adsorption energy (−1.52 eV) is higher than SO_2. Following this, SO_2 gas molecules migrate into the vacuum region adjacent to the $^{\bullet}$OH

https://doi.org/10.1021/acs.jpcc.5c07658
J. Phys. Chem. C 2026, 130, 2538−2548

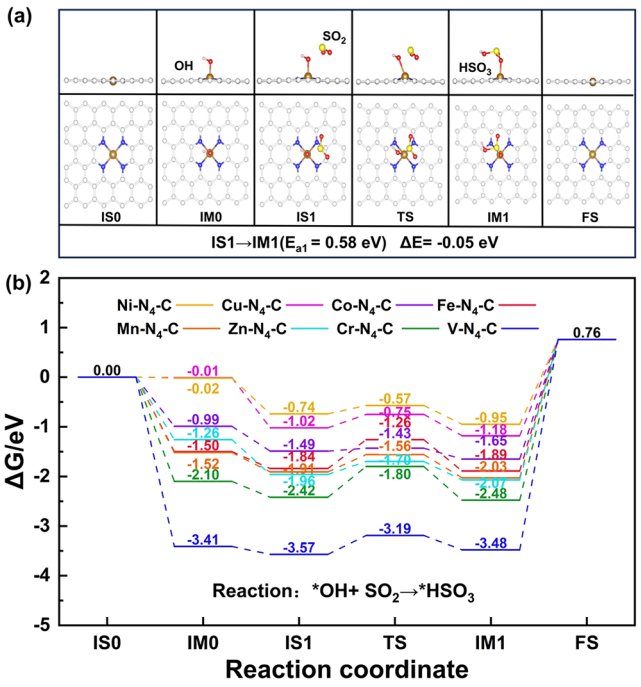

Figure 2. (a) Reaction process of SO_2 oxidation by $^{\bullet}OH$ over Fe−N_4−C catalyst. (b) Energy variation diagram of the reaction process on 8 types of TM-N_4−C catalysts. The initial state (IS0, energy zero) is defined as the clean catalyst plus gaseous $^{\bullet}OH$ and SO_2. The final state (FS) corresponds to the clean catalyst with HSO_3 in the gas phase. C, N, O, H, S, and Fe atoms are represented in white, blue, red, pink, yellow, and brown, respectively.

radical, where their presence affects the originally stable $^{\bullet}OH$ adsorption configuration on the Fe−N_4−C surface. As the reaction proceeds, SO_2 molecules initiate an attack on the oxygen atom, resulting in progressive weakening of the O−Fe interaction while the S−O bonding strengthens. The cleavage of the O−Fe bond is accompanied by the formation of an O−S bond. Eventually, the O atom in HSO_3 adsorbs onto the Fe metal active site of the catalyst, resulting in the final state structure (IM1). Despite retained O−Fe bonding, the oxygen adsorbate transforms from $^{\bullet}OH$ to HSO_3, exhibiting enhanced adsorption strength (ΔE_{ads} = −1.13 eV, from −1.52 eV to −2.65 eV). This process proceeds with an activation barrier (E_a) of 0.58 eV and releases 0.05 eV of energy, confirming its thermodynamic favorability. Our calculations reveal similar reaction pathways for HSO_3 formation across eight TM-N_4−C (TM = V ∼ Zn) catalysts, while the transition state configurations vary significantly among different metal centers. Detailed reaction processes for $^{\bullet}OH$ radical and SO_2 conversion to HSO_3 on all eight catalytic systems are presented in Figures S3−S9.

To better analyze the reaction mechanism of SO_2 oxidation by $^{\bullet}OH$ radicals, the energy profiles for HSO_3 formation on eight TM-N_4−C catalysts are presented in Figure 2b. We set the zero-point energy state by summing the energies of the $^{\bullet}OH$ radical, SO_2 molecule, and catalyst framework. Meanwhile, the enforcement of proton conservation constraints across all intermediate configurations enables the construction of a detailed energy step diagram of the reaction pathway. Figure 2b shows that all eight TM-N_4−C catalysts exhibit low reaction barriers for the $^{\bullet}OH$-mediated SO_2 oxidation process. The energy difference between the initial (IS0) and final (FS) states corresponds to the net energy change of the reaction: gaseous $^{\bullet}OH$ + SO_2 → gaseous HSO_3. From Table S1, it can be observed that the energy barriers for the oxidation of SO_2 by $^{\bullet}OH$ radicals on the eight TM-N_4−C catalysts exhibit minor differences. This suggests that it is difficult to investigate the reaction mechanism of $^{\bullet}OH$ radicals oxidizing NO in the presence of SO_2 through this process, screening catalysts based on these computational results becomes challenging. Therefore, we further calculated the reaction process of HSO_3 oxidizing NO on the eight TM-N_4−C catalysts.

3.2.2. Reaction Pathway of NO Oxidation by HSO_3 on SACs. Based on our calculations, the reaction mechanisms across the eight types of SACs are similar. Therefore, to further probe the catalytic mechanism, we take the Fe−N_4−C catalyst as an example to elaborate in detail the oxidation pathway of NO by HSO_3 on SACs (Figure 3a). Initially, HSO_3 adsorbs

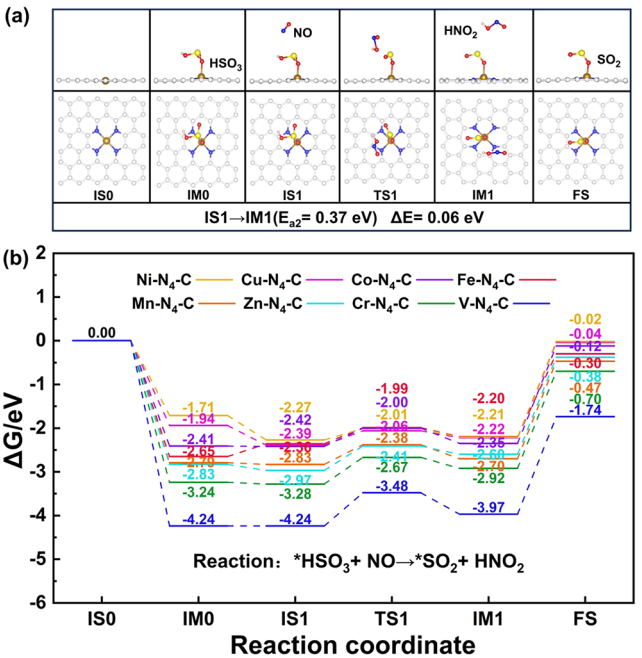

Figure 3. (a) Reaction process of NO oxidation by HSO_3 over Fe−N_4−C catalyst. (b) Energy variation diagram of the reaction process on 8 types of TM-N_4−C catalysts. The initial state (IS0, energy zero) is defined as the clean catalyst plus gaseous HSO_3 and NO. The final state (FS) corresponds to the catalyst with SO_2 adsorbed and HNO_2 in the gas phase. C, N, O, H, S, and Fe atoms are represented in white, blue, red, pink, yellow, and brown, respectively.

onto the metal site of the catalyst, forming the intermediate IM0. Subsequently, an NO molecule enters the vacuum layer above HSO_3, forming the initial reaction state IS1. As the reaction proceeds, the NO molecule attacks the S−OH bond, leading to its cleavage. The $^{\bullet}OH$ group then interacts with the NO molecule, generating the product HNO_2. This step follows an Eley−Rideal mechanism, where gaseous NO directly attacks adsorbed HSO_3. During S−OH cleavage, the newly formed HNO_2 is kinetically expelled from the surface, while SO_2 remains adsorbed due to its retained metal coordination. Crucially, the desorption barrier of SO_2 (e.g., 0.30 eV on Fe−N_4−C) is significantly lower than that of HNO_2 in the conventional SO_2-free pathway (∼0.98 eV)—this switch in the desorption-limited step is the key to the SO_2 promotion effect.[26] Upon completion of the reaction, only SO_2 remains

https://doi.org/10.1021/acs.jpcc.5c07658
J. Phys. Chem. C 2026, 130, 2538−2548

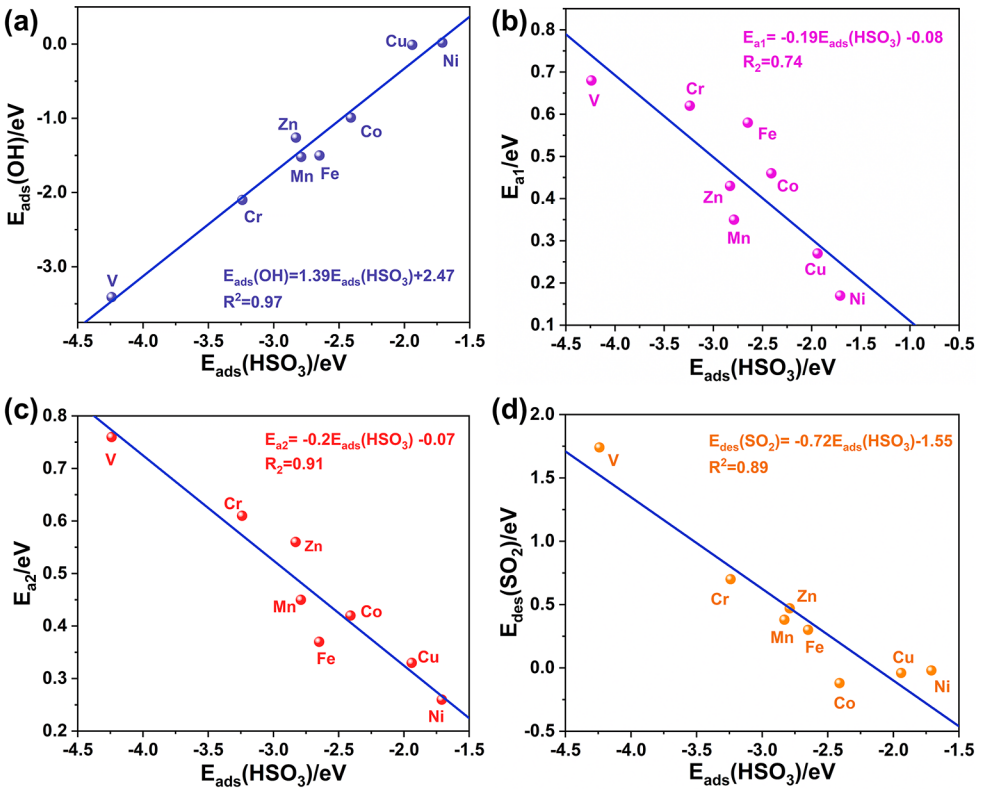

Figure 4. Correlation analyses of (a) E_{ads} (•OH) vs E_{ads} (HSO_3), (b) E_{a1} vs E_{ads} (HSO_3), (c) E_{a2} vs E_{ads} (HSO_3) and (d) E_{des} (SO_2) vs E_{ads} (HSO_3).

adsorbed on the metal site Fe. The energy barrier (E_a) for this reaction is 0.37 eV, and the entire process requires an energy absorption of 0.06 eV from the surroundings. After the reaction, SO_2 remains adsorbed on Fe−N_4−C, with a desorption energy barrier (E_{des}) of 0.3 eV. The catalytic oxidation of NO by HSO_3 on other SACs is depicted in Figures S10−S16.

The catalytic oxidation removal of NO fundamentally relies on the generation of highly oxidative active species on the catalyst surface, which react with NO molecules to form higher-valent nitrogen oxides that are more easily eliminated. Previous studies have demonstrated the catalytic oxidation of NO using O_2-based strong oxidants on single-atom catalysts (SACs),[41] where the rate-determining step (RDS) exhibits a high energy barrier of 1.33 eV. Other researchers have investigated NO oxidation via H_2O_2-activated intermediate radicals on Fe−N_4−C catalysts, achieving a significantly lower reaction barrier of 0.14 eV. However, in this process, HNO_2 remains adsorbed on the catalyst surface, with a desorption energy as high as 0.98 eV, which hinders the regeneration of active sites and thus impedes further catalytic cycles.[42,43] Additionally, studies on Fe−N_4−C catalysts have explored the influence of Hg on NO removal, providing valuable insights for this work regarding the effect of SO_2 on NO oxidation.[44] Compared to conventional catalytic approaches, the strategy of utilizing SO_2 to promote NO oxidation significantly reduces the energy barrier required for the reaction. Moreover, the weak adsorption energy of SO_2 on the catalyst prevents it from occupying active sites, thereby accelerating the overall reaction kinetics.

To more intuitively analyze the energy changes during the entire reaction process, Figure 3b presents the energy profiles of the complete reaction on eight TM-N_4−C catalysts. The zero-energy state was defined as the sum of energies for the HSO_3 sulfur-containing intermediate, NO molecule, and the catalyst surface. Proton conservation was maintained for each intermediate state to ensure well-defined relative energies with respect to the ground state, enabling the construction of a comprehensive reaction energy ladder diagram. By comparing the reaction energy barriers (E_a) and desorption barriers (E_{des}), we observed that for Fe−N_4−C, Co−N_4−C, Mn−N_4−C, Cu−N_4−C, Zn−N_4−C, and Ni−N_4−C catalysts, although both E_a and E_{des} values were relatively small, the reaction barriers slightly exceeded the desorption barriers. Consequently, the activity limit of these catalytic systems was determined by the reaction barrier magnitude. In contrast, for Cr−N_4−C and V−N_4−C catalysts, the desorption barriers were marginally higher than the reaction barriers, making E_{des} the limiting factor for overall activity. These analyses reveal that an optimal catalyst must possess balanced reaction and desorption barriers, as either excessively high E_a or E_{des} would adversely impact catalytic performance. Detailed energy variations for the HSO_3-mediated NO oxidation process on all eight TM-N_4−C catalysts are summarized in Table S2. It is worth noting that this focus shift from HSO_3 formation (rate-limiting in Fe−N_4−C) to the HSO_3 + NO → SO_2 + HNO_2 step aligns with our screening goal. HSO_3 formation barriers vary minimally across catalysts (Figure 2b), providing poor screening power. In contrast, the NO oxidation step shows significant, systematic variations in reaction barriers (Figure 3b), making it the descriptor-sensitive key step for universal activity prediction.

3.3. Correlation Analysis

There exists an intrinsic correlation between reaction kinetics and the thermodynamics of catalytic processes.[45−47] Therefore, we studied the correlation between reaction kinetics and thermodynamics through the thermodynamic evaluation and

https://doi.org/10.1021/acs.jpcc.5c07658
J. Phys. Chem. C 2026, 130, 2538−2548

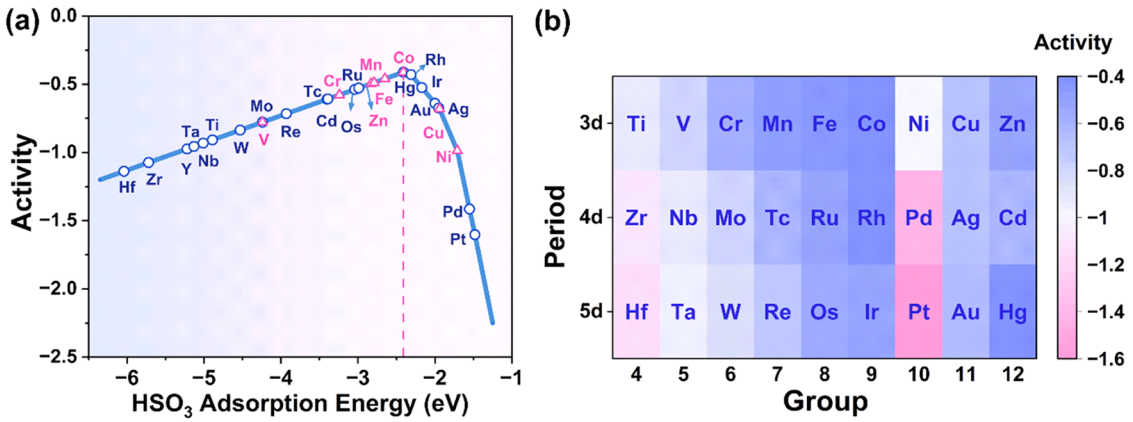

Figure 5. (a) Volcano plot of reaction activity of NO oxidation as a function of HSO_3 adsorption energy with 28 SACs. (b) Reaction activity of different SACs predicted using the heat map.

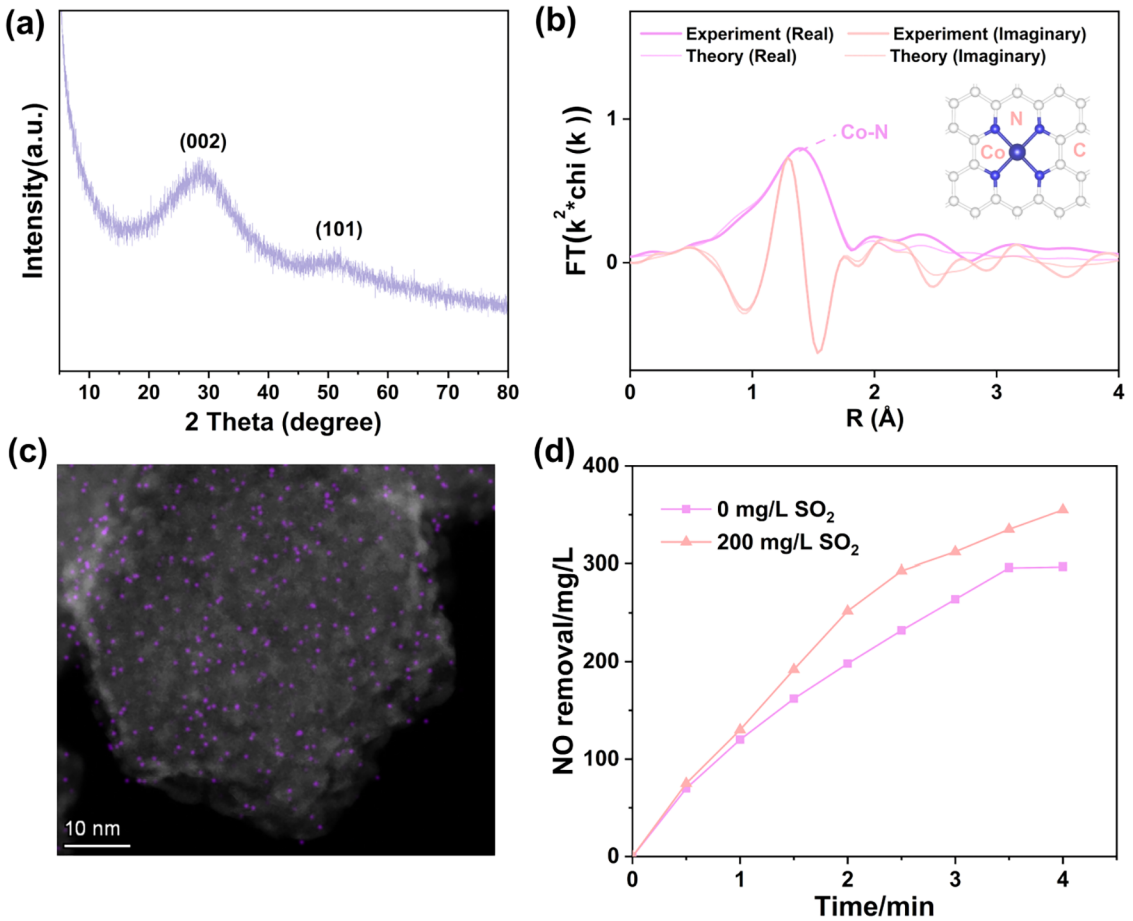

Figure 6. (a) XRD patterns of Co−N_4−C. (b) Co K-edge EXAFS fitting of Co−N_4−C. (c) HAADF-STEM image of Co−N_4−C. The bright spots correspond to isolated cobalt single atoms. (d) The effect of different concentrations of SO_2 on the oxidation of NO on Co−N_4−C.

mechanistic interpretation of the reaction pathway. Given that the adsorption energy has been widely recognized as a robust descriptor for predicting catalytic activity in heterogeneous catalysis,[48,49] we investigated the linear relationships between the adsorption energy of HSO_3 and several key parameters: the adsorption energy of $^{\bullet}OH$, the reaction energy barrier (E_{a1} and E_{a2}), and the desorption energy barrier (E_{des} (SO_2)). As illustrated in Figure 4a, the adsorption energy of HSO_3 exhibits a positive linear correlation with that of $^{\bullet}OH$, indicating that as the HSO_3 adsorption energy increases, the $^{\bullet}OH$ adsorption energy also rises. Figure 4b−d present the respective relationships between HSO_3 adsorption energy and (i) the activation barrier E_{a1}, (ii) the reaction barrier E_{a2}, and (iii) the SO_2 desorption energy (E_{des} (SO_2)). Significantly, the HSO_3 adsorption energy shows a negative linear correlation in all three cases, meaning that as the HSO_3 adsorption energy increases, these energy barriers decrease. Through this analysis, a crucial catalytic principle emerges: enhancing the adsorption strength of HSO_3 increases the $^{\bullet}OH$ adsorption energy but simultaneously reduces the reaction energy barriers (E_{a1} and

https://doi.org/10.1021/acs.jpcc.5c07658
J. Phys. Chem. C 2026, 130, 2538−2548

E_{a2}) and the SO_2 desorption energy barrier (E_{des} (SO_2)), thereby modulating the overall catalytic activity. This dual effect suggests that neither excessively strong nor excessively weak adsorption is conducive to optimizing catalytic performance. Therefore, to achieve highly reactive catalysts, the adsorption energy of HSO_3 must be regulated within an optimal range.

3.4. Microkinetic Analysis

The aforementioned analysis demonstrates linear correlations between the HSO_3 adsorption energy and the reaction energy barriers (E_{a1} and E_{a2}) as well as the SO_2 desorption energy barrier (E_{des} (SO_2)) during the reaction process. Consequently, the HSO_3 adsorption energy serves as an effective descriptor for accurately predicting catalytic activity. Here, Sabatier analysis was employed to determine the maximum achievable reaction rates of different catalysts,[50,51] thereby providing an effective assessment of their intrinsic catalytic performance. To better simulate realistic flue gas conditions, the catalytic oxidation activity of HSO_3 toward NO was evaluated at T = 400 K and $P_{H_2O_2}$ = 0.05 bar, generating an activity volcano plot (Figure 5a). The constructed 1D volcano model, using HSO_3 adsorption energy as the descriptor, positioned eight single-atom catalysts (SACs) on the plot. Analysis reveals that the activity limits for catalysts on the left and right branches of the volcano are governed by the $^{\bullet}OH$ radical activation energy and the combined effects of the NO oxidation barrier (E_{a2}) and SO_2 desorption energy (E_{des} (SO_2)), respectively. Among all SACs, Co−N_4−C exhibits optimal performance, located nearest to the volcano apex which corresponds to an HSO_3 adsorption energy of −2.41 eV. Therefore, among various single-atom catalysts, those with HSO_3 adsorption energies approaching −1.50 eV exhibit enhanced theoretical reaction rates for NO oxidation.

To extend the predictive scope, this study additionally computed the HSO_3 adsorption energies on 4d and 5d transition metal SACs (isoelectronic to the Ti ∼ Zn series), obtaining their theoretically predicted values of their catalytic activity. As shown in Figure 5a, the results indicate that Co−N_4−C exhibit superior catalytic activity among the 28 evaluated SACs. Moreover, to better visualize the periodic trends in single-atom catalyst activity, we employed a heatmap analysis to predict the reactivity of various SACs. As illustrated in Figure 5b, the x-axis corresponds to the group number of the metal elements, while the y-axis represents their respective periods. The color intensity directly correlates with catalytic activity, with darker shades indicating higher performance. Our analysis reveals a positive correlation between group number and catalytic activity in groups 4−9, while group 10 metals display markedly reduced reactivity. Furthermore, within the same group, 3d transition metals consistently demonstrate enhanced activity compared to their 4d and 5d counterparts. Although the volcano plot in Figure 5a is presented at fixed conditions for clarity, the underlying full microkinetic model is capable of predicting activity trends under varying operational parameters. As shown in Supporting Figure S17, the model successfully captures the variation of the turnover frequency (TOF) with total pressure and temperature for the optimal Co−N_4−C catalyst, confirming its robustness beyond the simplified Sabatier analysis.

3.5. Experimental Analysis

The volcano plot analysis predicted that the Co−N_4−C catalyst would exhibit excellent activity for NO oxidation by HSO_3. To verify this theoretical prediction, we conducted systematic fixed-bed experiments to investigate the promotional effect of SO_2 on NO oxidation. Prior to catalytic testing, comprehensive structural characterizations were performed. The X-ray diffraction pattern of Co−N_4−C (Figure 6a) shows characteristic (002) and (101) reflections of graphitic carbon at 28° and 50°(2θ), confirming the intact graphite framework. The absence of diffraction signals from metallic Co or cobalt oxides suggests atomic-scale dispersion of cobalt species. To further verify this, extended X-ray absorption fine structure (EXAFS) measurements were performed to probe the local coordination environment of Co atoms. As shown in Figure 6b, the optimal fitting analysis of the EXAFS spectra for the Co−N_4−C reveals that the Co atom is coordinated with four N atoms, which is consistent with our DFT calculations. Moreover, the high-angle annular dark-field-scanning transmission electron microscopy (HAADF-STEM) image (Figure 6c) clearly reveals uniformly distributed isolated bright spots on the carbon support, directly demonstrating the Co species are dominantly present in the form of single atoms rather than clusters or nanoparticles.

To investigate the effect of SO_2 on NO oxidation, the catalytic performance was evaluated under controlled conditions (140 °C, 500 ppm of NO, 2 mol/L H_2O_2) with varying SO_2 concentrations (0 and 200 ppm). As shown in Figure 6d, we obtained the variation curves of NO removal amount over time under these two different SO_2 concentrations. During the reaction, the NO removal efficiency with 200 ppm of SO_2 was notably higher than in the absence of SO_2 (0 ppm). Remarkably, the results demonstrate that 200 ppm of SO_2 promotes NO oxidation by facilitating HSO_3 generation and lowering desorption energy barriers. This observation agrees well with the volcano plot prediction, thereby validating the accuracy of the activity volcano plot screening using HSO_3 adsorption energy as the descriptor. The close theory-experiment agreement validates the physical relevance of our computational model. The gas-phase treatment of NO/SO_2 in DFT is a justified simplification for the high-concentration, continuous-flow fixed-bed conditions. Although the model simplifies NO adsorption, it correctly captures the activity trend governed by the HSO_3 adsorption energy—the key descriptor that correlates directly with the observed SO_2-promotion effect. Thus, the model is validated both by its predictive volcano-plot screening and by its consistency with macroscopic catalytic performance. Together, these experiments provide proof-of-concept validation for the SO_2-promotion mechanism, confirming the HSO_3-mediated pathway on the optimal Co−N_4−C catalyst. While focusing on validating the fundamental promotion effect, comprehensive testing across multiple TM-N_4−C catalysts would directly verify the volcano plot ranking. Such systematic experimental screening is a natural extension of the framework established in this work.

3.6. Electronic Characteristics

Next, to further investigate the role of electronic properties in regulating the catalytic activity of single-atom catalysts (SACs),[52−54] particularly their influence on the adsorption strength of sulfur-containing intermediates like HSO_3, we systematically analyzed the electronic characteristics of 28 different SACs. Theoretical calculations revealed clear linear correlations between the HSO_3 adsorption energy and two key electronic descriptors: As shown in Figure 7a, the Bader charge

https://doi.org/10.1021/acs.jpcc.5c07658
J. Phys. Chem. C 2026, 130, 2538−2548

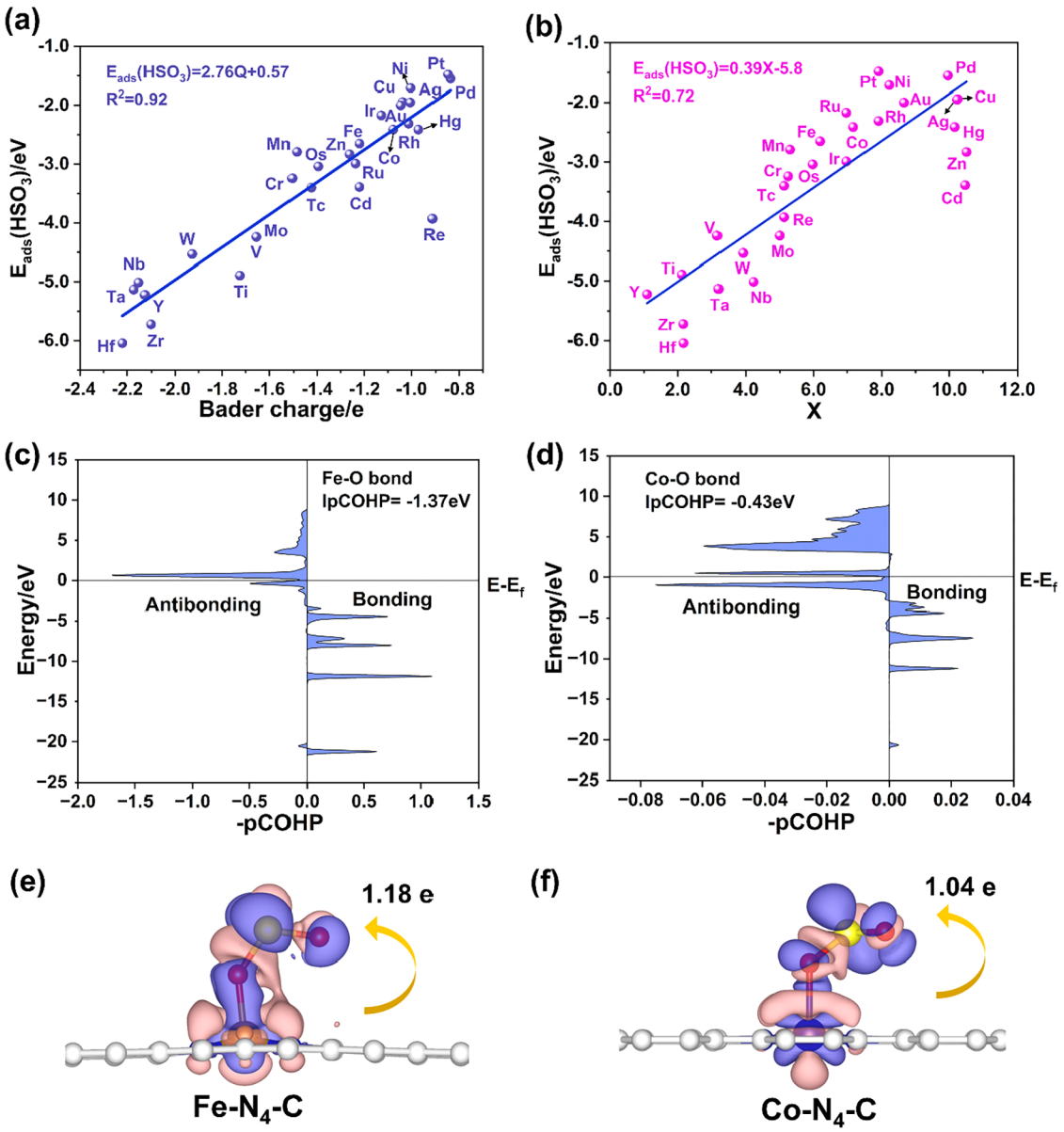

Figure 7. Linear relationship of (a) E_{ads} (HSO_3) vs Bader charge (b) E_{ads} (HSO_3) vs electronegativity (X). COHP analysis between different SACs and SO_2: (c) Fe−N_4−C and (d) Co−N_4−C. Electronic density difference between different SACs and SO_2: (e) Fe−N_4−C and (f) Co−N_4−C. Contour lines in the plots are drawn at 0.001 e Å^{-3} intervals. Red and blue areas represent electron gain and loss, respectively. White, blue, red, and yellow spheres represent C, N, O, and S, respectively.

of the metal active site exhibits a significant correlation with HSO_3 adsorption energy. Similarly, Figure 7b demonstrates that the electronegativity of the catalyst also follows a linear dependence with adsorption strength. These quantitative relationships provide crucial insights for the rational design of high-efficiency NO oxidation catalysts through electronic structure modulation.

Our previous studies revealed that SO_2 enhances the H_2O_2-mediated oxidation of NO primarily by modifying product desorption properties.[26] For example, on Fe−N_4−C catalysts, SO_2 participation lowers the desorption barrier from 0.98 to 0.30 eV by converting the final product from HNO_2 to SO_2, thereby, significantly boosting catalytic activity. To probe the underlying mechanisms of SO_2 desorption, we employed Crystal Orbital Hamiltonian Population (COHP)[55] and Electron Density Difference (EDD) analyses.[56] Figure 7c,d present the COHP analysis of the interaction between SO_2 and the catalyst surfaces for Fe−N_4−C and Co−N_4−C systems, respectively. The COHP results reveal that the Fe−N_4−C catalyst exhibits minimal antibonding orbital occupancy, yielding a strong Fe-SO_2 interaction (1.37 eV). In contrast, for the Co−N_4−C catalyst system, the antibonding orbital population is significantly larger, leading to a weaker interaction energy of only 0.43 eV between the Co atom and the SO_2 molecule. This reduced adsorption strength facilitates the desorption process of SO_2. Based on these findings, we conclude that weaker adsorption strength between the catalyst surface and SO_2 facilitates easier desorption of reaction products, thereby enhancing the overall catalytic activity. The COHP analyses of other SACs (Figure S18) further reveal that, with the exception of the V−N_4−C catalyst system, all other investigated catalysts demonstrate comparatively weaker bonding strengths with SO_2 molecules.

https://doi.org/10.1021/acs.jpcc.5c07658
J. Phys. Chem. C 2026, 130, 2538−2548

At the same time, to gain deeper insight into the electronic origins of the varying bonding strengths between different SACs and SO_2, we performed electron density difference (EDD) analyses on both Fe−N_4−C and Co−N_4−C catalyst systems (Figure 7e,f). The electron density difference (EDD) analysis shows that pink regions correspond to electron gain, while blue regions indicate electron loss. For the Fe−N_4−C catalyst system, the Fe atom is surrounded by a blue region, demonstrating its role as an electron donor during the catalytic process, with the majority of transferred electrons migrating to the adsorbed SO_2 molecule. In contrast, although the Co atom in the Co−N_4−C system is similarly enveloped by a blue region, the extent of electron transfer is significantly less pronounced compared to the Fe system. A portion of the donated electrons is instead redistributed to the coordinating nitrogen atoms in the immediate vicinity. Due to greater electron donation to SO_2 on Fe−N_4−C, the Fe-SO_2 interaction (1.37 eV) is stronger than the Co−SO_2 interaction (0.43 eV), explaining the easier desorption of SO_2 from Co−N_4−C and its enhanced overall catalytic activity. The above analysis elucidates the origin of bonding strength variations between different SACs and SO_2 at the microscopic electronic level, while also providing guidance for subsequent exploration of catalysts with higher reactivity. The EDD analysis of other SACs is presented in Figure S19. Additionally, Table S3 summarizes the charge transfer and bond length variations between different SACs and SO_2 molecules.

4. CONCLUSION

In summary, this study systematically investigated the SO_2-promoted NO oxidation mechanism over single-atom catalysts. Through density functional theory (DFT) calculations, we first examined the reaction pathway of SO_2 with $^{\bullet}OH$ radicals to form HSO_3 intermediates. The results indicate that the energy barriers for HSO_3 formation are similar across all eight SACs, making it difficult to screen catalysts. Subsequently, the HSO_3-mediated NO oxidation process on these catalysts was explored to determine the corresponding reaction energy barriers and thermodynamic profiles. Based on the Brønsted-Evans−Polanyi (BEP) relationship, we identified the HSO_3 adsorption energy as a key descriptor, which exhibits linear correlations with $^{\bullet}OH$ adsorption energy, reaction barriers, and SO_2 desorption energy. Following the Sabatier principle, we constructed a volcano plot to evaluate the catalytic activity of HSO_3-assisted NO oxidation, successfully predicting the performance of 28 SACs (3d, 4d, and 5d metals). Among them, Co−N_4−C exhibits the highest activity near the volcano peak. Fixed-bed experiments confirmed that SO_2 enhances NO oxidation over Co−N_4−C, validating the theoretical predictions from the volcano plot. Furthermore, we analyzed the relationship between Bader charge, electronegativity, and the descriptor, revealing strong linear trends that enable catalytic performance prediction based on electronic structure. Finally, crystal orbital Hamiltonian population (COHP) and electron density difference (EDD) analyses were employed to elucidate the bonding interactions and charge redistribution between SO_2 and Co/Fe−N_4−C surfaces, establishing a microscopic electronic structure−macroscopic activity correlation for rational catalyst design. This work not only proposes a novel SO_2-enhanced strategy for NO removal but also provides a universal descriptor and theoretical framework for screening high-performance NO removal catalysts. We anticipate that this research will provide novel theoretical insights for pollutant removal strategies and a robust framework for identifying high-performance NO oxidation catalysts.

■ ASSOCIATED CONTENT

Supporting Information

The Supporting Information is available free of charge at https://pubs.acs.org/doi/10.1021/acs.jpcc.5c07658.

Convergence tests (Figure S1), Experimental setup (Figure S2), computational details and energy calculation methods (S1), microkinetic modeling parameters (S2), materials and catalyst synthesis procedures (S3, S4), reaction pathway figures for all catalysts (Figures S3−S16), predicted TOF trends with pressure and temperature (Figure S17), COHP and EDD analysis (Figures S18−S19), energy barrier (E_{a1}), reaction heat (ΔE), and imaginary frequency for SO_2 oxidation to HSO_3 by $^{\bullet}OH$; energy barrier (E_{a2}), reaction heat (ΔE) and imaginary frequency for the oxidation of NO by HSO_3; charge transfer (Q) of the central TM and the bond length (d) between TM and SO_2 gas molecule on different SACs (Tables S1−S3) (PDF)

■ AUTHOR INFORMATION

Corresponding Author

Weijie Yang − *Department of Power Engineering, North China Electric Power University, Baoding 071003 Hebei, China; Hebei Key Laboratory of Low Carbon and High-Efficiency Power Generation Technology, North China Electric Power University, Baoding 071003 Hebei, China;* orcid.org/0000-0002-0232-1129; Email: yangwj@ncepu.edu.cn

Authors

Zhengyang Gao − *Department of Power Engineering, North China Electric Power University, Baoding 071003 Hebei, China; Hebei Key Laboratory of Low Carbon and High-Efficiency Power Generation Technology, North China Electric Power University, Baoding 071003 Hebei, China*

Ze Liu − *Department of Power Engineering, North China Electric Power University, Baoding 071003 Hebei, China; Hebei Key Laboratory of Low Carbon and High-Efficiency Power Generation Technology, North China Electric Power University, Baoding 071003 Hebei, China*

Chu Wang − *Department of Power Engineering, North China Electric Power University, Baoding 071003 Hebei, China; Hebei Key Laboratory of Low Carbon and High-Efficiency Power Generation Technology, North China Electric Power University, Baoding 071003 Hebei, China*

Ziwei Miao − *Department of Power Engineering, North China Electric Power University, Baoding 071003 Hebei, China; Hebei Key Laboratory of Low Carbon and High-Efficiency Power Generation Technology, North China Electric Power University, Baoding 071003 Hebei, China*

Tongao Yao − *Department of Power Engineering, North China Electric Power University, Baoding 071003 Hebei, China; Hebei Key Laboratory of Low Carbon and High-Efficiency Power Generation Technology, North China Electric Power University, Baoding 071003 Hebei, China*

Jianghao Cai − *Department of Power Engineering, North China Electric Power University, Baoding 071003 Hebei, China; Hebei Key Laboratory of Low Carbon and High-Efficiency Power Generation Technology, North China*

https://doi.org/10.1021/acs.jpcc.5c07658
J. Phys. Chem. C 2026, 130, 2538−2548

Electric Power University, Baoding 071003 Hebei, China; orcid.org/0000-0003-1077-1733

Yixiao Sun − *Department of Power Engineering, North China Electric Power University, Baoding 071003 Hebei, China; Hebei Key Laboratory of Low Carbon and High-Efficiency Power Generation Technology, North China Electric Power University, Baoding 071003 Hebei, China*

Yuanzheng Qu − *Department of Power Engineering, North China Electric Power University, Baoding 071003 Hebei, China; Hebei Key Laboratory of Low Carbon and High-Efficiency Power Generation Technology, North China Electric Power University, Baoding 071003 Hebei, China*

Complete contact information is available at: https://pubs.acs.org/10.1021/acs.jpcc.5c07658

Author Contributions

Z.G.: Project administration, funding acquisition, software. Z.L.: Visualization, writing—original draft. C.W.: Writing—review and editing. Z.M.: Visualization. T.Y.: Visualization. J.C.: Visualization. Y.S.: Methodology, Data curation, validation. Y.Q.: Investigation, data curation. W.Y.: Supervision, conceptualization, funding acquisition, writing—review and editing.

Notes

The authors declare no competing financial interest.

■ ACKNOWLEDGMENTS

This work was funded by the National Natural Science Foundation of China (Nos. 52176104 and 52006073).

■ REFERENCES

(1) Li, X.; Ren, S.; Chen, Z.; Wang, M.; Chen, L.; Chen, H.; Yin, X. A Review of Mn-Based Catalysts for Abating NO_x and CO in Low-Temperature Flue Gas: Performance and Mechanisms. *Molecules* **2023**, *28* (19), No. 6885.

(2) Dong, J.; Gao, Z.; Yang, W.; Li, A.; Ding, X. Adsorption characteristics of Co-anchored different graphene substrates toward O_2 and NO molecules. *Appl. Surf. Sci.* **2019**, *480*, 779−791.

(3) Talib, S. H.; Hussain, S.; Baskaran, S.; Lu, Z.; Li, J. Chromium single-atom catalyst with graphyne support: a theoretical study of NO oxidation and reduction. *ACS Catal.* **2020**, *10* (20), 11951−11961.

(4) Getman, R. B.; Schneider, W. F. DFT-based coverage-dependent model of Pt-catalyzed NO oxidation. *ChemCatChem* **2010**, *2* (11), 1450−1460.

(5) Hao, R.; Zhao, Y.; Yuan, B.; Zhou, S.; Yang, S. Establishment of a novel advanced oxidation process for economical and effective removal of SO_2 and NO. *J. Hazard. Mater.* **2016**, *318*, 224−232.

(6) Liu, X.; Wang, Ca.; Zhu, T.; Lv, Q.; Li, Y.; Che, D. Simultaneous removal of NO_x and SO_2 from coal-fired flue gas based on the catalytic decomposition of H_2O_2 over $Fe_2(MoO_4)_3$. *Chem. Eng. J.* **2019**, *371*, 486−499.

(7) Chen, L.; Ren, D.; Hou, X.; Zhang, J.; Wu, Y.; Wang, Y.; Hu, C.; Duan, P.; Li, C.; Chiang, C.; He, C.; Lu, Q. Asymmetric oxygen vacancy-enriched Mn_2O_3@ CeO_2 for NO oxidation with excellent low-temperature activity and boosted SO_2-resistance. *Appl. Catal., B* **2024**, *340*, No. 123202.

(8) Wang, F.; Cai, Q.; Gao, J.; He, X.; Ji, Y.; Shen, B. Synthesis of hollow structured $MnCeO_x$@ $PrCeO_x$ catalyst for low temperature NH_3-SCR with enhanced SO_2 resistance. *Appl. Surf. Sci.* **2025**, *685*, No. 162067.

(9) Chen, W.; Qu, Z.; Huang, W.; Hu, X.; Yan, N. Novel effect of SO_2 on selective catalytic oxidation of slip ammonia from coal-fired flue gas over IrO_2 modified Ce−Zr solid solution and the mechanism investigation. *Fuel* **2016**, *166*, 179−187.

(10) Chen, H.; Wang, C.; Zhang, J.; Shi, Y.; Liu, Y.; Qian, Z. NO_x attenuation in flue gas by $\bullet OH/SO_4^{\bullet-}$-based advanced oxidation processes. *Environ. Sci. Pollut. Res.* **2020**, *27* (30), 37468−37487.

(11) Mahbub, P.; Duke, M. Scalability of advanced oxidation processes (AOPs) in industrial applications: A review. *J. Environ. Manage.* **2023**, *345*, No. 118861.

(12) Gligorovski, S.; Strekowski, R.; Barbati, S.; Vione, D. Environmental implications of hydroxyl radicals (•OH). *Chem. Rev.* **2015**, *115* (24), 13051−13092.

(13) Chen, L.; Xu, Z. W.; He, C.; Wang, Y. G.; Liang, Z. Y.; Zhao, Q. X.; Lu, Q. Gas-phase total oxidation of nitric oxide using hydrogen peroxide vapor over Pt/TiO_2. *Appl. Surf. Sci.* **2018**, *457*, 821−830.

(14) Wu, B.; Xiong, Y. A novel low-temperature NO removal approach with •OH from catalytic decomposition of H_2O_2 over $La_{1-x}Ca_xFeO_3$ oxides. *J. Chem. Technol. Biotechnol.* **2018**, *93* (1), 43−53.

(15) Zhu, C.; Nie, Y.; Zhao, S.; Fan, Z.; Liu, F.; Li, A. Constructing surface micro-electric fields on hollow single-atom cobalt catalyst for ultrafast and anti-interference advanced oxidation. *Appl. Catal., B* **2022**, *305*, No. 121057.

(16) Yang, W. J.; Chen, L. G.; Zhou, B. H.; Jia, Z. H.; Liu, X. S.; Liu, Y. F.; Li, H.; Gao, Z. Y. NO oxidation using H_2O_2 at a single-atom iron catalyst. *J. Phys. Chem. C* **2023**, *127* (27), 13011−13020.

(17) Yang, X.-F.; Wang, A.; Qiao, B.; Li, J.; Liu, J.; Zhang, T. Single-atom catalysts: a new frontier in heterogeneous catalysis. *Acc. Chem. Res.* **2013**, *46* (8), 1740−1748.

(18) Li, L.; Chang, X.; Lin, X.; Zhao, Z.-J.; Gong, J. Theoretical insights into single-atom catalysts. *Chem. Soc. Rev.* **2020**, *49* (22), 8156−8178.

(19) Zhang, N. Q.; Ye, C. L.; Yan, H.; Li, L. C.; He, H.; Wang, D. S.; Li, Y. D. Single-atom site catalysts for environmental catalysis. *Nano Res.* **2020**, *13* (12), 3165−3182.

(20) Yuan, Q.; Cheng, L. Theoretical study on NO oxidation using single metal atom catalysis embedded graphene with N_4 vacancy. *Compu. Theor. Chem.* **2023**, *1230*, No. 114390.

(21) Liu, X. S.; Gao, Z. Y.; Huang, H. Y.; Yan, G.; Huang, T. F.; Chen, C.; Yang, W. J.; Ding, X. L. Simultaneous catalytic oxidation of nitric oxide and elemental mercury by single-atom Pd/g-C_3N_4 catalyst: A DFT study. *Mol. Catal.* **2020**, *488*, No. 110901.

(22) Yang, W.; Gao, Z.; Liu, X.; Ma, C.; Ding, X.; Yan, W. Directly catalytic reduction of NO without NH_3 by single atom iron catalyst: A DFT calculation. *Fuel* **2019**, *243*, 262−270.

(23) Wang, H.; Zhang, B.; Yang, H.; Bao, Q.; Wu, B. New insights on the effects of SO_2 on NO oxidation from flue gas with H_2O_2 vapor over Fe_2O_3/SiO_2. *Process Saf. Environ. Prot.* **2022**, *165*, 138−150.

(24) Wu, B.; Xiong, Y.; Ge, Y. Simultaneous removal of SO_2 and NO from flue gas with OH from the catalytic decomposition of gas-phase H_2O_2 over solid-phase $Fe_2(SO_4)_3$. *Chem. Eng. J.* **2018**, *331*, 343−354.

(25) Jia, S.; Pu, G.; Gao, J.; Yuan, C. Oxidation-absorption process for simultaneous removal of NO_x and SO_2 over Fe/Al_2O_3@ SiO_2 using vaporized H_2O_2. *Chemosphere* **2022**, *291*, No. 133047.

(26) Gao, Z. Y.; Sun, Y. X.; Miao, Z. W.; Qu, Y. Z.; Li, X.; Chen, S. L.; Yang, W. J. Promotion mechanism of SO_2 on the catalytic oxidation of NO by H_2O_2. *J. Environ. Chem. Eng.* **2025**, *13* (2), No. 115439.

(27) Blöchl, P. E. Projector augmented-wave method. *Phys. Rev. B* **1994**, *50* (24), No. 17953.

(28) Perdew, J. P.; Burke, K.; Ernzerhof, M. Generalized gradient approximation made simple. *Phys. Rev. Lett.* **1996**, *77* (18), No. 3865.

(29) Wu, Z.; Cohen, R. E. More accurate generalized gradient approximation for solids. *Phys. Rev. B* **2006**, *73* (23), No. 235116.

(30) Moellmann, J.; Grimme, S. DFT-D3 study of some molecular crystals. *J. Phys. Chem. C* **2014**, *118* (14), 7615−7621.

(31) Yang, W. J.; Huang, H. Y.; Liu, X. S.; Ren, J. N.; Ma, K.; Pan, Z. H.; Ding, Z.; Ding, X. L.; Gao, Z. Y. Screening the activity of single-atom catalysts for the catalytic oxidation of sulfur dioxide with a kinetic activity model. *Chem. Commun.* **2020**, *56* (78), 11657−11660.

(32) Henkelman, G.; Arnaldsson, A.; Jónsson, H. A fast and robust algorithm for Bader decomposition of charge density. *Comput. Mater. Sci.* **2006**, *36* (3), 354−360.
(33) Dronskowski, R.; Bloechl, P. E. Crystal orbital Hamilton populations (COHP): energy-resolved visualization of chemical bonding in solids based on density-functional calculations. *J. Phys. Chem. A* **1993**, *97* (33), 8617−8624.
(34) Maintz, S.; Deringer, V. L.; Tchougréeff, A. L.; Dronskowski, R. LOBSTER: A tool to extract chemical bonding from plane-wave based DFT. *J. Comput. Chem.* **2016**, *37*, 1030−1035, DOI: 10.1002/jcc.24300.
(35) Henkelman, G.; Uberuaga, B. P.; Jónsson, H. A climbing image nudged elastic band method for finding saddle points and minimum energy paths. *J. Chem. Phys.* **2000**, *113* (22), 9901−9904.
(36) Heyden, A.; Bell, A. T.; Keil, F. J. Efficient methods for finding transition states in chemical reactions: Comparison of improved dimer method and partitioned rational function optimization method. *J. Chem. Phys.* **2005**, *123* (22), No. 224101.
(37) Bendavid, L. I.; Carter, E. A. CO_2 adsorption on Cu_2O (111): a DFT+ U and DFT-D study. *J. Phys. Chem. C* **2013**, *117* (49), 26048−26059.
(38) Molani, F.; Asadpour, M.; Jafari, M.; Sadeghi, M.; Khatibinasab, R. Structural, electronic, and mechanical properties of transition metal porphyrin-like graphenes, and their application in hydroxylation of methane. *Appl. Phys. A* **2024**, *130* (11), No. 774.
(39) Yang, W.; Feng, Y.; Chen, X.; Wu, C.; Wang, F.; Gao, Z.; Liu, Y.; Ding, X.; Li, H. Understanding Trends in the NO Oxidation Activity of Single-Atom Catalysts. *J. Environ. Chem. Eng.* **2022**, *10* (6), No. 108744.
(40) Hung, H.-M.; Hoffmann, M. R. Oxidation of gas-phase SO_2 on the surfaces of acidic microdroplets: Implications for sulfate and sulfate radical anion formation in the atmospheric liquid phase. *Environ. Sci. Technol.* **2015**, *49* (23), 13768−13776.
(41) Tang, Y.; Zhou, J.; Chen, W.; Chai, H.; Li, Y.; Feng, Z.; Dai, X. Theoretical evaluation on single-atom Fe doped divacancy graphene for catalytic CO and NO oxidation by O_2 molecules. *Mol. Catal.* **2019**, *476*, No. 110524.
(42) Yang, W.; Chen, L.; Zhou, B.; Jia, Z.; Liu, X.; Liu, Y.; Li, H.; Gao, Z. NO oxidation using H_2O_2 at a single-atom iron catalyst. *J. Phys. Chem. C* **2023**, *127* (27), 13011−13020.
(43) Dong, S.; Wang, J.; Li, C.; Liu, H.; Gao, Z.; Wu, C.; Yang, W. Simultaneous catalytic oxidation mechanism of NO and Hg^0 over single-atom iron catalyst. *Appl. Surf. Sci.* **2023**, *609*, No. 155298.
(44) Yang, W.; Chen, X.; Chen, L.; Feng, Y.; Wu, C.; Ding, X.; Gao, Z.; Liu, Y.; Li, H. Design of single-atom catalysts for Hg^0 oxidation using H_2O_2. *J. Phys. Chem. C* **2022**, *126* (50), 21234−21242.
(45) Zhang, J.; Tao, H.; Kuang, M.; Yang, H.; Cai, W.; Yan, Q.; Mao, Q.; Liu, B. Advances in thermodynamic-kinetic model for analyzing the oxygen evolution reaction. *ACS Catal.* **2020**, *10* (15), 8597−8610.
(46) Bligaard, T.; Nørskov, J. K.; Dahl, S.; Matthiesen, J.; Christensen, C. H.; Sehested, J. The Brønsted−Evans−Polanyi relation and the volcano curve in heterogeneous catalysis. *J. Catal.* **2004**, *224* (1), 206−217.
(47) Van Santen, R. A.; Neurock, M.; Shetty, S. G. Reactivity theory of transition-metal surfaces: a Brønsted−Evans−Polanyi linear activation energy−free-energy analysis. *Chem. Rev.* **2010**, *110* (4), 2005−2048.
(48) Huang, H. C.; Li, J.; Zhao, Y.; Chen, J.; Bu, Y. X.; Cheng, S. B. Adsorption energy as a promising single-parameter descriptor for single atom catalysis in the oxygen evolution reaction. *J. Mater. Chem. A* **2021**, *9* (10), 6442−6450.
(49) Xie, W. L.; Cui, B.; Liu, D. S.; Huang, H. C.; Yang, C. L. Rational Design of Covalent Organic Frameworks-Based Single Atom Catalysts for Oxygen Evolution Reaction and Oxygen Reduction Reaction. *Molecules* **2025**, *30* (7), No. 1505.
(50) Falsig, H.; Hvolbæk, B.; Kristensen, I. S.; Jiang, T.; Bligaard, T.; Christensen, C. H.; Norskov, J. K. Trends in the catalytic CO oxidation activity of nanoparticles. *Angew. Chem., Int. Ed.* **2008**, *47* (26), No. 4835.
(51) Medford, A. J.; Vojvodic, A.; Hummelshoj, J. S.; Voss, J.; Abild-Pedersen, F.; Studt, F.; Bligaard, T.; Nilsson, A.; Norskov, J. K. From the Sabatier principle to a predictive theory of transition-metal heterogeneous catalysis. *J. Catal.* **2015**, *328*, 36−42.
(52) Zhang, T.; Walsh, A. G.; Yu, J.; Zhang, P. Single-atom alloy catalysts: structural analysis, electronic properties and catalytic activities. *Chem. Soc. Rev.* **2021**, *50* (1), 569−588.
(53) Giulimondi, V.; Mitchell, S.; Pérez-Ramírez, J. Challenges and opportunities in engineering the electronic structure of single-atom catalysts. *ACS Catal.* **2023**, *13* (5), 2981−2997.
(54) Zhuo, H.-Y.; Zhang, X.; Liang, J.-X.; Yu, Q.; Xiao, H.; Li, J. Theoretical understandings of graphene-based metal single-atom catalysts: stability and catalytic performance. *Chem. Rev.* **2020**, *120* (21), 12315−12341.
(55) Dronskowski, R.; Bloechl, P. E. Crystal orbital Hamilton populations (COHP): energy-resolved visualization of chemical bonding in solids based on density-functional calculations. *J. Phys. Chem. A* **1993**, *97* (33), 8617−8624.
(56) Cremer, D.; Kraka, E. Chemical bonds without bonding electron density—does the difference electron-density analysis suffice for a description of the chemical bond? *Angew. Chem., Int. Ed.* **1984**, *23* (8), 627−628.